

Design of diamond microcavities for single photon frequency down-conversion

Z. Lin, S. G. Johnson, A. W. Rodriguez and M. Loncar

School of Engineering and Applied Sciences, Harvard University, Cambridge MA, 02138

zlin@seas.harvard.edu

Abstract: We propose monolithic diamond cavities that can be used to convert color-center Fock-state single photons from emission wavelengths to telecommunication bands. We present a detailed theoretical description of the conversion process, analyzing important practical concerns such as nonlinear phase shifts and frequency mismatch. Our analysis predicts sustainable power requirements ($\lesssim 1$ W) for a chipscale nonlinear device with high conversion efficiencies.

© 2018 Optical Society of America

OCIS codes: (000.0000) General.

References and links

1. P. Michler, A. Kiraz, C. Becher, W. V. Schoenfeld, P. M. Petroff, L. Zhang, E. Hu, and A. Imamoglu. A quantum dot single-photon turnstile device. *Science*, 290:2282–2285, 2000.
2. M. Pelton, C. Santori, J. Vučković, B. Zhang, G. S. Solomon, J. Plant, and Y. Yamamoto. Efficient source of single photons: a single quantum dot in a micropost microcavity. *Phys. Rev. Lett.*, 89(23):233602, 2002.
3. L. M. Duan and H. J. Kimble. Scalable photonic quantum computation through cavity-assisted interactions. *Phys. Rev. Lett.*, 94(12):127902, 2004.
4. J. I. Cirac, P. Zoller, H. J. Kimble, and H. Mabuchi. Quantum state transfer and entanglement distribution among distant nodes in a quantum network. *Phys. Rev. Lett.*, 78:3221–3224, 1997.
5. A. Kuhn, M. Hennrich, and G. Rempe. Deterministic single-photon source for distributed quantum networking. *Phys. Rev. Lett.*, 89(6):067901, 2002.
6. L. Childress, J. M. Taylor, A. S. Sorensen, and M. D. Lukin. Fault-tolerant quantum communication based on solid-state photon emitters. *Phys. Rev. Lett.*, 96:070504, 2006.
7. H. J. Kimble. The quantum internet. *Nature*, 453:1023–1030, 2008.
8. C. Kurtsiefer, S. Mayer, P. Zarda, and H. Weinfurter. Stable solid-state source of single photons. *Phys. Rev. Lett.*, 85:290–293, 2000.
9. A. Beveratos, R. Brouri, T. Gacoin, A. Villing, J. Poizat, and P. Grangier. Single photon quantum cryptography. *Phys. Rev. Lett.*, 89:187901, 2002.
10. T. M. Babinec, B. J. Hausmann, M. Khan, Y. Zhang, J. R. Maze, P. R. Hemmer, and M. Loncar. A diamond nanowire single-photon source. *Nat. Nano.*, 5:195–199, 2010.
11. F. Jelezko, T. Gaebel, I. Popa, A. Gruber, and J. Wrachtrup. Observation of coherent oscillations in a single electron spin. *Phys. Rev. Lett.*, 92:076401, Feb 2004.
12. Steven Prawer and Andrew D. Greentree. Diamond for quantum computing. *Science*, 320(5883):1601–1602, 2008.
13. M. V. Gurudev Dutt, L. Childress, L. Jiang, E. Togan, J. Maze, F. Jelezko, A. S. Zibrov, P. R. Hemmer, and M. D. Lukin. Quantum register based on individual electronic and nuclear spin qubits in diamond. *Science*, 316(5829):1312–1316, 2007.
14. P. Neumann, N. Mizuochi, F. Rempp, P. Hemmer, H. Watanabe, S. Yamasaki, V. Jacques, T. Gaebel, F. Jelezko, and J. Wrachtrup. Multipartite entanglement among single spins in diamond. *Science*, 320(5881):1326–1329, 2008.
15. M. W. McCutcheon and M. Loncar. Design of a silicon nitride photonic crystal nanocavity with a quality factor of one million for coupling to a diamond nanocrystal. *Opt. Express*, 16(23):19136, 2008.

16. Igor Aharonovich, Chunyuan Zhou, Alastair Stacey, Julius Orwa, Stefania Castelletto, David Simpson, Andrew D. Greentree, François Treussart, Jean-François Roch, and Steven Praver. Enhanced single-photon emission in the near infrared from a diamond color center. *Phys. Rev. B*, 79:235316, Jun 2009.
17. I. Aharonovich, S. Castelletto, B. C. Johnson, J. C. McCallum, and S. Praver. Engineering chromium-related single photon emitters in single crystal diamonds. *New Journal of Physics*, 13(045015), 2011.
18. L. J. Rogers, K. D. Jahnke, L. Marseglia, C. Müller, B. Naydenov, H. Schauffert, C. Kranz, T. Teraji, J. Isoya, L. P. McGuinness, and F. Jelezko. Creation of multiple identical single photon emitters in diamond. *ArXiv e-prints*, Oct 2013.
19. Matthias Leifgen, Tim Schrder, Friedemann Gdeke, Robert Riemann, Valentin Mtilton, Elke Neu, Christian Hepp, Carsten Arend, Christoph Becher, Kristian Lauritsen, and Oliver Benson. Evaluation of nitrogen- and silicon-vacancy defect centres as single photon sources in quantum key distribution. *New Journal of Physics*, 16(2):023021, 2014.
20. Elke Neu, Mario Agio, and Christoph Becher. Photophysics of single silicon vacancy centers in diamond: implications for single photon emission. *Opt. Express*, 20(18):19956–19971, Aug 2012.
21. Christian Hepp, Tina Müller, Victor Waselowski, Jonas N. Becker, Benjamin Pingault, Hadwig Sternschulte, Doris Steinmüller-Nethl, Adam Gali, Jeronimo R. Maze, Mete Atatüre, and Christoph Becher. Electronic structure of the silicon vacancy color center in diamond. *Phys. Rev. Lett.*, 112:036405, Jan 2014.
22. A. Sipahigil, K.D. Jahnke, L.J. Rogers, T. Teraji, J. Isoya, A.S. Zibrov, F. Jelezko, and M.D. Lukin. Indistinguishable photons from separated silicon-vacancy centers in diamond. *Phys. Rev. Lett.*, 113(113602), 2014.
23. D. Englund, B. Shields, K. Rivoire, F. Hatami, J. Vučković, H. Park, and M. D. Lukin. Deterministic coupling of a single nitrogen vacancy center to a photonic crystal cavity. *Nano Lett.*, 10:3922–3926, 2010.
24. Wolters et al. Enhancement of the zero phonon line emission from a single nitrogen vacancy center in a nanodiamond via coupling to a photonic crystal cavity. *Appl. Phys. Lett.*, 97:141108, 2010.
25. T. van der Sar et al. Deterministic nanoassembly of a coupled quantum emitter-photonic crystal cavity system. *Appl. Phys. Lett.*, 98:193103, 2011.
26. N. P. de Leon et al. Tailoring light-matter interaction with a nanoscale plasmon resonator. *Phys. Rev. Lett.*, 108:226803, 2012.
27. A. Faraon, P. E. Barclay, C. Santori, K. M. C. Fu, and R. G. Beausoleil. Resonant enhancement of the zero-phonon emission from a color centre in a diamond cavity. *Nat. Photonics*, 12:1578, 2012.
28. B. M. Hausmann et al. Integrated diamond networks for quantum nanophotonics. *Nano Lett.*, 12:1578, 2012.
29. A. Faraon, C. Santori, Z. Huang, V. M. Acosta, and R. G. Beausoleil. Coupling of nitrogen-vacancy centers to photonic crystal cavities in monocrystalline diamond. *Phys. Rev. Lett.*, 109:033604, 2012.
30. J. Riedrich-Moeller et al. One- and two-dimensional photonic crystal microcavities in single crystal diamond. *Nat. Nano.*, 7, 2012.
31. M. J. Burek et al. Free-standing mechanical and photonic nanostructures in single-crystal diamond. *Nano Lett.*, 12:6084, 2012.
32. B. J. M. Hausmann, B. J. Shields, Q. Quan, Y. Chu, N. P. de Leon, R. Evans, M. J. Burek, A. S. Zibrov, M. Markham, D. J. Twitchen, H. Park, M. D. Lukin, and M. Loncar. Coupling of nv centers to photonic crystal nanobeams in diamond. *Nano Lett.*, 13:5791 – 5796, 2013.
33. Michael J. Burek, Yiwen Chu, Madelaine S.Z. Liddy, Parth Patel, Jake Rochman, Srujan Meesala, Wooyoung Hong, Qimin Quan, Mikhail D. Lukin, and Marko Loncar. High quality-factor optical nanocavities in bulk single-crystal diamond. *Nat. Comm.*, 5:5718, 2014.
34. B. J. M. Hausmann, I. Bulu, V. Venkataraman, P. Deotare, and M. Loncar. Diamond nonlinear photonics. *Nature Photonics*, 8:369 – 374, 2014.
35. Murray W. McCutcheon, Darrick E. Chang, Yinan Zhang, Mikhail D. Lukin, and Marko Loncar. Broadband frequency conversion and shaping of single photons emitted from a nonlinear cavity. *Opt. Express*, 17:22689, 2009.
36. I. Agha, M. Davanco, B. Thurston, and K. Srinivasan. Low-noise chip-based frequency conversion by four-wave-mixing bragg scattering in Si_3N_4 waveguides. *Opt. Lett.*, 37:2997, 2012.
37. Y. Huang, V. Velev, and P. Kumar. Quantum frequency conversion in nonlinear microcavities. *Opt. Lett.*, 38:2119–2121, 2013.
38. P. D. Drummond. Electromagnetic quantization in dispersive inhomogeneous nonlinear dielectrics. *Phys. Rev. A*, 42:6845–6857, 1990.
39. D. Ramirez, A. W. Rodriguez, H. Hashemi, J. D. Joannopoulos, M. Soljacic, and S. G. Johnson. Degenerate four-wave mixing in triply-resonant nonlinear kerr cavities. *Phys. Rev. A*, 83:033834, 2011.
40. Alejandro Rodriguez, Marin Soljačić, J. D. Joannopoulos, and Steven G. Johnson. $\chi^{(2)}$ and $\chi^{(3)}$ harmonic generation at a critical power in inhomogeneous doubly resonant cavities. *Opt. Express*, 15(12):7303–7318, 2007.
41. Steven G. Johnson, Attila Mekis, Shanhui Fan, and J. D. Joannopoulos. Molding the flow of light. *Computing Sci. Eng.*, 3(6):38–47, 2001.
42. Jonas Hansryd, Peter A. Andrekson, Mathias Westlund, Jie Li, and Per-Olof Hedekvist. Fiber-based optical parametric amplifiers and their applications. *IEEE J. Sel. Topics in Quantum Electronics*, 8(3), 2002.
43. Robert W. Boyd. *Nonlinear Optics*. Academic Press, California, 1992.

44. Elke Neu, David Steinmetz, Janine Riedrich-Moller, Stefan Gsell, Martin Fischer, Matthias Schreck, and Christoph Becher. Single photon emission from silicon-vacancy colour centres in chemical vapour deposition nano-diamonds on iridium. *New J. Phys.*, 13(025012), 2011.
 45. M. J. Burek, N. P. de Leon, B. J. Shields, B. J. M. Hausmann, Y. Chu, Q. Quan, A. S. Zibrov, H. Park, M. D. Lukin, and M. Loncar. Free-standing mechanical and photonic nanostructures in single-crystal diamond. *Nano Lett.*, 12:6084–6089, 2012.
 46. M. Hillery. An introduction to the quantum theory of nonlinear optics. *Acta Physica Slovaca*, 1:1–80, 2009.
 47. Steven G. Johnson and J. D. Joannopoulos. Block-iterative frequency-domain methods for Maxwell’s equations in a planewave basis. *Opt. Express*, 8(3):173–190, 2001.
-

1. Introduction

Solid-state single photon emitters are an important step towards scalable quantum information technology [1, 2, 3]. A single emitter resonantly coupled to a high-finesse microcavity offers a natural functional unit to realize important applications in quantum cryptography and communication sciences [4, 5, 6, 7]. In recent years, there has been strong interest in the negatively-charged nitrogen-vacancy (NV^-) color center in diamond for coherent control of its optical and spin properties [8, 9, 10]. However, although the NV center has long spin coherence times, of importance for many quantum applications [11, 12, 13, 14], its fluorescence spectrum is stretched over a huge incoherent phonon side-band, that constitutes 96% of the entire emission [15]. More recently, other color centers in diamond were explored as a possible alternative to NV [16, 17]; for example, the ZPL of silicon-vacancy (SiV) center (ZPL ~ 738 nm) is found to be much stronger than that of NV, constituting 70% of the spectrum [18]. Recent studies have also established the fundamental attributes of the SiV emitter including its electronic structure and polarization states [19, 20, 21, 18] as well as single photon indistinguishability from these sources [22], validating SiV as a strong candidate for chip-based quantum optical applications.

On the fabrication side, many important steps have been taken to integrate diamond color centers into chip-scale devices, including hybrid approaches [23, 24, 25, 26] in which diamond samples with color centers are juxtaposed to cavities fabricated in non-diamond materials, as well as monolithic all-diamond approaches [27, 28, 29, 30, 31, 32, 33] in which the cavity itself is hewn out of single crystal diamond. The latter, though technically more challenging, has proven to be a superior platform for diamond-based quantum photonics. On the other hand, the utility of third-order nonlinearity $\chi^{(3)}$ in diamond microphotonic devices has been explored in a recent work [34] which demonstrates the generation of frequency combs by parametric oscillators fabricated in single crystal diamond thin films. Such capabilities open up an intriguing possibility – to build a monolithic all-diamond emitter/frequency-converter in a single cavity design that efficiently collects and down-converts the color-center photon into low-loss telecom frequency channels for long distance communication.

Chipscale frequency down-conversion of quantum signals has been discussed by various authors for different material systems [35, 36, 37]. In particular, Ref. [37] has proposed a silicon nitride (SiN) micro-ring resonator that can convert *few-photons* coherent light states from visible to telecom frequencies. Here, we propose a monolithic diamond structure that can be used to convert color-center *Fock-state single* photons from emission wavelengths to telecommunication bands ($\sim 1.5 \mu\text{m}$). We present a detailed theoretical description of the conversion process, analyzing important practical concerns such as nonlinear phase shifts and frequency mismatch, which were not considered in previous papers. Additionally, we present an efficient design technique for realizing perfect phase-matching in nonlinear optical cavities. Our analysis predicts sustainable power requirements for a chipscale nonlinear device with high conversion efficiencies achievable at total pump powers below one Watt.

Although our theoretical analysis is generally valid for *any* color center, we primarily tailor our cavity designs to the SiV emitter. Specifically, we consider a single SiV emitter implanted

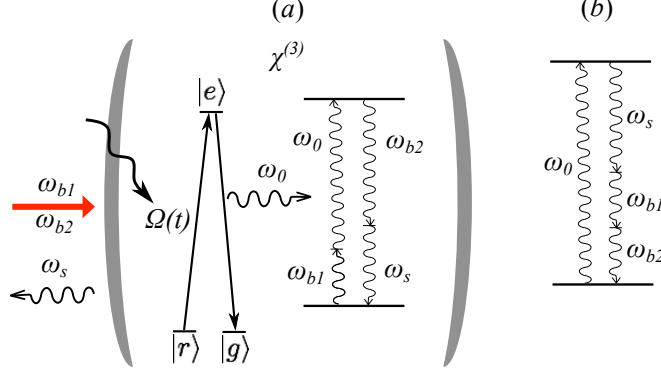


Fig. 1. (a) Schematic of an emitter-cavity system in which a single emitter is embedded in a nonlinear $\chi^{(3)}$ cavity supporting four resonant modes at frequencies $\{\omega_{0c}, \omega_{sc}, \omega_{b1c}, \omega_{b2c}\}$. The eigenstructure of the emitter is represented by a simplified three-level system with states $|r\rangle$, $|e\rangle$, $|g\rangle$. A laser trigger with frequency ω_{re} and intensity $\propto |\Omega|^2$ addresses the emitter states $|r\rangle$ and $|e\rangle$. The photon released from the emitter is collected by the cavity and down-converted to telecom through the four-wave mixing Bragg scattering process (FWM-BS). The latter process obeys the frequency-matching relation $\omega_s + \omega_{b2} = \omega_0 + \omega_{b1}$, where ω_0 and ω_s are the frequencies of the emitter and telecom signals, and ω_{b1} and ω_{b2} are the frequencies of the NIR and telecom pump lasers respectively. (b) Alternatively, the single photon (ω_0) can be down-converted by the difference frequency generation (DFG) process in which it is broken up into one signal (ω_s) and two pump photons (ω_{b1} , ω_{b2}), satisfying the frequency relation: $\omega_0 - \omega_{b1} - \omega_{b2} = \omega_s$. Here, we choose the two pump photons to be degenerate, $\omega_{b1} = \omega_{b2} = \omega_b$.

in a high-Q microcavity. In the case of triggered single photon emission, the electronic structure of the emitter can be well-approximated by a simple three-level diagram [35] with the electronic states denoted by $|r\rangle$, $|e\rangle$ and $|g\rangle$ (Fig. 1a). To start with, the emitter is prepared in the state $|r\rangle$. An external trigger excites the system to the state $|e\rangle$ which subsequently decays to the ground $|g\rangle$, emitting a photon of frequency ω_0 into the surrounding cavity. The photon release is followed by frequency down-conversion (within the same cavity) via a nonlinear wave-mixing process which utilizes the inherent third order susceptibility $\chi^{(3)}$ of diamond.

A common scheme for $\chi^{(3)}$ -based frequency down-conversion is four-wave mixing Bragg-scattering (FWM-BS) [36, 37], in which the incoming photon at emitter frequency ω_0 is scattered by coherent pump lasers at frequencies ω_{b1} and ω_{b2} to yield an outgoing photon at frequency ω_s , satisfying the frequency matching condition $\omega_0 + \omega_{b1} = \omega_s + \omega_{b2}$ (Fig. 1a). Alternatively, the down-conversion can be realized by a difference frequency generation (DFG) scheme in which the SiV emitter photon is directly broken up into one signal and two pump photons, with frequencies satisfying the relation $\omega_0 - \omega_{b2} - \omega_{b1} = \omega_s$ (Fig. 1b). In this paper, we present carefully designed diamond microcavities that can enhance frequency down-conversion via FWM-BS or DFG. In particular, we design our cavities to host four resonant modes (ω_{0c} , ω_{sc} , ω_{b1c} , ω_{b2c}) that respect the frequency matching conditions, $\omega_{0c} + \omega_{b1c} \approx \omega_{sc} + \omega_{b2c}$ for FWM-BS and $\omega_{0c} - \omega_{b1c} - \omega_{b2c} \approx \omega_{sc}$ for DFG.

In what follows, we mainly focus our discussion on FWM-BS; however, the analysis is equally applicable to DFG, for which we briefly discuss design specifications, efficiency and power predictions. In our analysis, we take into account the effects of frequency mismatch as well as those of self and cross-phase modulation (ignored in the earlier work [37]) and find that even in their presence, maximum efficiency can be achieved by appropriate power inputs. We

found that the maximum efficiencies can vary from 30 % to 90%, depending on the internal quantum efficiency of the color center (i.e., the ratio of radiative to non-radiative decay) and the quality factor of the cavity mode at the emitter frequency. Our cavity designs ensure that these efficiencies can be achieved by input pump powers lower than one Watt.

2. Theoretical considerations

The effective Hamiltonian of the emitter-cavity system including the dissipative terms has the following form (in the Schrödinger picture):

$$\begin{aligned}
\mathcal{H} = & \hbar\omega_{0c} \hat{a}_0^\dagger \hat{a}_0 + \hbar\omega_{sc} \hat{a}_s^\dagger \hat{a}_s + \hbar\omega_0 \hat{\sigma}_{ee} + \hbar\omega_r \hat{\sigma}_{rr} \\
& - \sum_{\mu,b} \hbar\omega_{\mu c} \alpha_{\mu b} |a_b|^2 \hat{a}_\mu^\dagger \hat{a}_\mu \\
& + \sum_l \hbar\omega_{lc} (1 - \alpha_{lb} |a_b|^2) \hat{a}_l^\dagger \hat{a}_l \\
& + \hbar\Omega(t) e^{-i\omega_{re}t} \hat{\sigma}_{er} + \hbar\Omega^*(t) e^{i\omega_{re}t} \hat{\sigma}_{re} \\
& + \hbar g_{ZPL} \hat{\sigma}_{eg} \hat{a}_0 + \hbar g_{ZPL} \hat{\sigma}_{ge} \hat{a}_0^\dagger \\
& - \hbar\beta \hat{a}_s^\dagger \hat{a}_0 e^{i(\omega_{b2} - \omega_{b1})t} - \hbar\beta^* \hat{a}_0^\dagger \hat{a}_s e^{-i(\omega_{b2} - \omega_{b1})t} \\
& + \hbar \sum_l \left(g_l \hat{\sigma}_{eg} \hat{a}_l + g_l \hat{\sigma}_{ge} \hat{a}_l^\dagger \right) \\
& - i\hbar \frac{\kappa_0}{2} \hat{a}_0^\dagger \hat{a}_0 - i\hbar \frac{\kappa_s}{2} \hat{a}_s^\dagger \hat{a}_s - i\hbar \sum_l \left(\frac{\kappa_l}{2} \hat{a}_l^\dagger \hat{a}_l \right) - i\hbar \frac{\gamma^{\text{NC}}}{2} \hat{\sigma}_{ee}.
\end{aligned} \tag{1}$$

Here, \hat{a} and \hat{a}^\dagger are annihilation and creation operators for the quantized cavity field at the emitter (0) and telecom (s) wavelengths, as well as at certain other wavelengths (l) that happen to fall within the phonon sidebands of the emission spectrum. The modal amplitudes of the classical laser pumps are denoted by a_b ($b \in \{b1, b2\}$) and are normalized so that $|a_b|^2$ is the energy in the b mode. $\hat{\sigma}_{ij} = |i\rangle\langle j|$ is the atomic operator connecting the j th and i th emitter states. $\Omega(t)$ is the Rabi frequency coupling the trigger pump and $r \leftrightarrow e$ transition whereas g_{ZPL} addresses the coupling between the ZPL decay and the 0th cavity mode. Similarly, the coefficients g_l describe the phonon sideband transitions that coincide with the cavity resonances at wavelengths l . Our model also includes self and cross-phase modulation via coefficients α introduced by the presence of the classical pump fields, whereas the strength of frequency conversion is described by β . These nonlinear coupling coefficients can be calculated from perturbation theory (see Appendix A). The leakage of each cavity mode is denoted by κ , which is related to the quality factor of the mode by $\kappa = \frac{\omega_c}{Q}$. γ^{NC} denotes the spontaneous decay rate of the emitter into continuum loss channels, including both radiative and non-radiative decays [35]. Note that in the above Hamiltonian, we have omitted nonlinear phase-modulation effects $\sim (\hat{a}^\dagger)^2 \hat{a}^2$ [38] owing to the quantum signals themselves, as these effects are vanishingly small at the single-photon level.

In addition to the Hamiltonian describing the quantum-mechanical degrees of freedom, we must also consider the coupled-mode equations for the classical degrees of freedom, namely the pump amplitudes a_{b1} and a_{b2} . These equations are given by [39]:

$$\begin{aligned}
\frac{da_{b1}}{dt} &= i\omega_{b1c} (1 - \alpha_{bb1} |a_{b1}|^2 - \alpha_{b1b2} |a_{b2}|^2) a_{b1} - \frac{a_{b1}}{\tau_{b1}} + \sqrt{\frac{2}{\tau_{sb1}}} P_{b1}, \\
\frac{da_{b2}}{dt} &= i\omega_{b2c} (1 - \alpha_{bb2} |a_{b2}|^2 - \alpha_{b1b2} |a_{b1}|^2) a_{b2} - \frac{a_{b2}}{\tau_{b2}} + \sqrt{\frac{2}{\tau_{sb2}}} P_{b2},
\end{aligned}$$

where P_{b1} and P_{b2} denote the powers of the incoming lasers coupling to the cavity modes ω_{b1c} and ω_{b2c} , with corresponding coupling lifetimes $\tau_{sb1} = \frac{2Q_{sb1}}{\omega_{b1c}}$ and $\tau_{sb2} = \frac{2Q_{sb2}}{\omega_{b2c}}$. Here, $\tau_{b1} = \frac{2Q_{sb1}}{\omega_{b1c}}$ and $\tau_{b2} = \frac{2Q_{sb2}}{\omega_{b2c}}$ are the overall lifetimes of the two cavity modes, which include all other sources of cavity losses (e.g. radiation and/or material absorption). Since one has the freedom to choose the frequencies (ω_{b1} , ω_{b2}) of the incoming pump lasers, it is always possible to operate under the resonant condition for the classical pumps,

$$\omega_{b1} = \omega_{b1c} (1 - \alpha_{bb1}|a_{b1}|^2 - \alpha_{b1b2}|a_{b2}|^2) \quad (2)$$

$$\omega_{b2} = \omega_{b2c} (1 - \alpha_{bb2}|a_{b2}|^2 - \alpha_{b1b2}|a_{b1}|^2), \quad (3)$$

which allows us to ignore effects associated with self- and cross-phase modulation [40, 39]. It follows that the steady-state energy in the classical cavity mode are given by $|a_{b1}|^2 = \frac{2\tau_{b1}^2}{\tau_{sb1}}P_{b1}$, $|a_{b2}|^2 = \frac{2\tau_{b2}^2}{\tau_{sb2}}P_{b2}$. Linear stability analysis [40, 39] also confirms that these solutions are stable.

The nonlinear coupling coefficients can be calculated from the perturbation theory [40, 41] (see also Appendix A):

$$\beta = \frac{3}{4} \sqrt{\omega_{0c} \omega_{sc} \left(\frac{2\tau_{b1}^2}{\tau_{sb1}} \frac{2\tau_{b2}^2}{\tau_{sb2}} \right) P_{b1} P_{b2}} \frac{\int dV \epsilon_0 \{ \chi_{xyxy} (\mathbf{E}_s^* \cdot \mathbf{E}_0) (\mathbf{E}_{b1} \cdot \mathbf{E}_{b2}^*) + \chi_{xyxy} (\mathbf{E}_s^* \cdot \mathbf{E}_{b1}) (\mathbf{E}_0 \cdot \mathbf{E}_{b2}^*) + \chi_{xyyx} (\mathbf{E}_s^* \cdot \mathbf{E}_{b2}^*) (\mathbf{E}_0 \cdot \mathbf{E}_{b1}) \}}{\sqrt{\int dV \epsilon_0 |\mathbf{E}_0|^2} \sqrt{\int dV \epsilon_s |\mathbf{E}_s|^2} \sqrt{\int dV \epsilon_{b1} |\mathbf{E}_{b1}|^2} \sqrt{\int dV \epsilon_{b1} |\mathbf{E}_{b2}|^2}}, \quad (4)$$

$$\alpha_{\mu b} = \frac{3}{4} \frac{\int dV \epsilon_0 \{ \chi_{xyxy} |\mathbf{E}_\mu|^2 |\mathbf{E}_b|^2 + \chi_{xyxy} |\mathbf{E}_\mu \cdot \mathbf{E}_b^*|^2 + \chi_{xyyx} |\mathbf{E}_\mu \cdot \mathbf{E}_b|^2 \}}{(\int dV \epsilon_0 |\mathbf{E}_\mu|^2) (\int dV \epsilon_b |\mathbf{E}_b|^2)}, \quad (5)$$

$$\alpha_{bb} = \frac{3}{8} \frac{\int dV \epsilon_0 \{ (\chi_{xyxy} + \chi_{xyyx}) |\mathbf{E}_b \cdot \mathbf{E}_b^*|^2 + \chi_{xyxy} |\mathbf{E}_b \cdot \mathbf{E}_b|^2 \}}{(\int dV \epsilon_b |\mathbf{E}_b|^2)^2}, \quad (6)$$

$$\alpha_{b1b2} = \frac{3}{4} \frac{\int dV \epsilon_0 \{ \chi_{xyxy} |\mathbf{E}_{b1} \cdot \mathbf{E}_{b2}^*|^2 + \chi_{xyxy} |\mathbf{E}_{b1} \cdot \mathbf{E}_{b2}|^2 + \chi_{xyyx} |\mathbf{E}_{b1}|^2 |\mathbf{E}_{b2}|^2 \}}{(\int dV \epsilon_{b1} |\mathbf{E}_{b1}|^2) (\int dV \epsilon_{b2} |\mathbf{E}_{b2}|^2)}. \quad (7)$$

The initial state of the emitter-cavity system is simply a tensor product of the emitter state $|r\rangle$ and the vacuum photonic states $|0_0\rangle$, $|0_s\rangle$ and $|0_l\rangle$:

$$|\Psi(0)\rangle = |r, 0_0, 0_s, 0_l\rangle. \quad (8)$$

We now proceed to solve the time evolution of Ψ under the Hamiltonian Eq. 1. It is easy to see that the initial state $|r, 0_0, 0_s, 0_l\rangle$ can only couple to states with one quantum of excitation, $|e, 0_0, 0_s, 0_l\rangle$ or $|g, n_0, n_s, n_l\rangle$, $n_0 + n_s + n_l = 1$. Therefore, it is sufficient to expand the total wavefunction as a superposition of these *single-excitation* states [35]:

$$\begin{aligned} |\Psi(t)\rangle &= c_r(t) e^{-i\omega_r t} |r, 0_0, 0_s, 0_l\rangle \\ &\quad + c_e(t) e^{-i\omega_0 t} |e, 0_0, 0_s, 0_l\rangle \\ &\quad + c_0(t) e^{-i\omega_0 t} |g, 1_0, 0_s, 0_l\rangle \\ &\quad + c_s(t) e^{-i\omega_s t} |g, 0_0, 1_s, 0_l\rangle \\ &\quad + \sum_l c_l(t) e^{-i\omega_l t} |g, 0_0, 0_s, 1_l\rangle. \end{aligned} \quad (9)$$

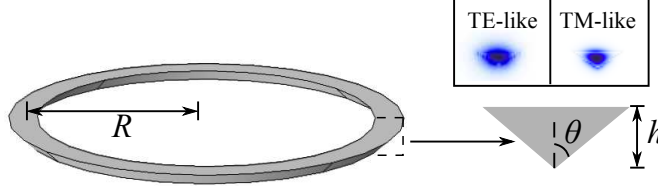


Fig. 2. Schematic of angle-etched diamond ring resonator (refractive index $n \approx 2.41$). The resonator has a radius R and a height h . The triangular cross-section has an etch-angle θ . E_r components of the fundamental TE0-like modes at frequencies $(\omega_{sc}, \omega_{b1c})$ and E_z components of the fundamental TM0-like modes at frequencies $(\omega_{0c}, \omega_{b2c})$ are also depicted in the picture.

Substituting Eq. 9 in the time-dependent Schrödinger equation, $i\hbar \frac{\partial |\Psi\rangle}{\partial t} = \mathcal{H} |\Psi\rangle$, leads to the following coupled equations of motion for the coefficients:

$$\dot{c}_r = -i\Omega^*(t)c_e \quad (10)$$

$$\dot{c}_e = -i\Omega(t)c_r - ig_{ZPL}c_0 - i \sum_l g_l c_l - \frac{\gamma^{\text{NC}}}{2} c_e \quad (11)$$

$$\dot{c}_0 = -i\delta_{0c}c_0 - ig_{ZPL}c_e - i\beta^* c_s - \frac{\kappa_0}{2} c_0 \quad (12)$$

$$\dot{c}_s = -i\delta_{sc}c_s - i\beta c_0 - \frac{\kappa_s}{2} c_s \quad (13)$$

$$\dot{c}_l = -ig_l c_e - \frac{\kappa_l}{2} c_l \quad (14)$$

$$\delta_{0c} = \omega_{0c} (1 - \alpha_{0b1}|a_{b1}|^2 - \alpha_{0b2}|a_{b2}|^2) - \omega_0 \quad (15)$$

$$\delta_{sc} = \omega_{sc} (1 - \alpha_{sb1}|a_{b1}|^2 - \alpha_{sb2}|a_{b2}|^2) - (\omega_0 + \omega_{b1} - \omega_{b2}). \quad (16)$$

The nonlinear detunings δ_{0c} and δ_{sc} , as defined by Eqs. 15–16, include the nonlinear phase shifts introduced by the pumps and are to be distinguished from the *bare* cavity detunings $\omega_{0c} - \omega_0$ and $\omega_{sc} + \omega_{b2c} - \omega_{0c} - \omega_{b1c}$ *without* the amplitude-dependent phase shifts.

In the regime where the trigger intensity $\sim \Omega$ and trigger rate $\sim \frac{d\Omega}{dt}$ are sufficiently small compared to the decay rates of the system, the probability coefficients c_i , $i \in \{e, 0, s, l\}$, follow the dynamics of c_r . Thus we can adiabatically eliminate the $e, 0, s, l$ degrees of freedom (see Appendix B), and arrive at the following expression for the conversion efficiency (defined as the percentage of triggers for which the excitations are ultimately down-converted to telecom [35]):

$$F = \frac{\int dt \kappa_{ss} |c_s|^2}{\int dt (\kappa_s |c_s|^2 + \kappa_0 |c_0|^2 + \sum_l \kappa_l |c_l|^2 + \gamma^{\text{NC}} |c_e|^2)} \quad (17)$$

$$= \frac{4C|\beta|^2 \kappa_0 \kappa_{ss}}{16|\beta|^4 + 4|\beta|^2 ((2+C)\kappa_0 \kappa_s - 8\delta_{0c} \delta_{sc}) + (4\delta_{0c}^2 + (1+C)\kappa_0^2) (4\delta_{sc}^2 + \kappa_s^2)}. \quad (18)$$

Here, C is the well-known cooperativity factor:

$$C = \frac{4g_{ZPL}^2}{\kappa_0 \left(\sum_l \frac{4g_l^2}{\kappa_l} + \gamma^{\text{NC}} \right)}, \quad (19)$$

which describes the *relative* strength of photon capture into the cavity 0th mode over the competing loss channels. Eq. 18 can be maximized by setting $\frac{\partial F}{\partial \delta_{0c}} = 0$, $\frac{\partial F}{\partial \delta_{sc}} = 0$, which yields:

$$F^{\max} = \left(1 + \frac{2}{C} - 2\sqrt{\frac{1}{C} + \frac{1}{C^2}}\right) \frac{Q_s}{Q_{ss}}, \quad (20)$$

under the constraints,

$$\delta_{0c}^{\text{crit}} = \delta_{sc}^{\text{crit}} = \pm \frac{1}{2} \sqrt{\frac{\kappa_0}{\kappa_s} \left(4\sqrt{1+C}|\beta|^2 - (1+C)\kappa_0\kappa_s\right)}. \quad (21)$$

A special situation arises when

$$\delta_{0c}^{\text{crit}} = \delta_{sc}^{\text{crit}} = 0, \quad (22)$$

in which case β is constrained by,

$$|\beta|^{\text{crit}} = \frac{(1+C)^{1/4}}{2} \sqrt{\frac{\omega_{0c}\omega_{sc}}{Q_0Q_s}}. \quad (23)$$

This scenario was already discussed in Ref. [35]. More generally, we can algebraically solve Eq. 21 together with Eqs. 2–3, to yield a set of critical powers and frequencies $\{\omega_{b1}^{\text{crit}}, P_{b1}^{\text{crit}}, \omega_{b2}^{\text{crit}}, P_{b2}^{\text{crit}}\}$. However, it must be noted that the above algebraic equations sometimes lead to negative or imaginary answers. Such cases indicate that the maximal efficiency is no longer given by Eq. 20; instead the critical efficiencies and powers are numerically found by directly setting

$$\frac{\partial F}{\partial P_{b1}} = 0, \quad \frac{\partial F}{\partial P_{b2}} = 0. \quad (24)$$

In the following sections, we will perform these calculations in the context of carefully designed realistic cavity systems.

3. Diamond Micro-ring Resonator

In this section, we consider concrete and realistic cavity designs for single photon frequency conversion based on a triangular ring resonator. We choose the triangular cross-section to take advantage of our recently developed angle-etched technique on monolithic bulk diamond [33]. The main advantage of angle-etched technique is its consistent yield and scalability compared to diamond-on-insulator thin-film techniques.

The most challenging task in our cavity design is to satisfy the frequency-matching relation $\omega_{0c} + \omega_{b1c} \approx \omega_{sc} + \omega_{b2c}$. One cannot straightforwardly apply conventional dispersion engineering techniques developed for FWM with closely-spaced frequencies [42] since, in our case, the conversion spans two very different frequency bands, NIR and telecom. One can do an extensive numerical search in the design space [37] but such an approach is time-consuming and computationally very expensive. In contrast, in the Appendix C, we describe a numerical/visualization technique that greatly simplifies the process of designing ring resonators that satisfy the frequency-matching condition. One such cavity is shown in Fig. 2. The ring has a radius $R = 14.4 \mu\text{m}$, a height $h = 414 \text{ nm}$ and a slant angle $\theta = 59^\circ$. Out of its many resonances, we will focus our attention on two fundamental transverse-electric-like (TE₀-like) modes in the telecom band, ($m_s = 95, \lambda_{sc} = 1.613 \mu\text{m}$) and ($m_{b1} = 79, \lambda_{b1c} = 1.806 \mu\text{m}$), and two fundamental transverse-magnetic-like (TM₀-like) modes in the NIR band, ($m_0 = 262, \lambda_{0c} = 738 \text{ nm}$)

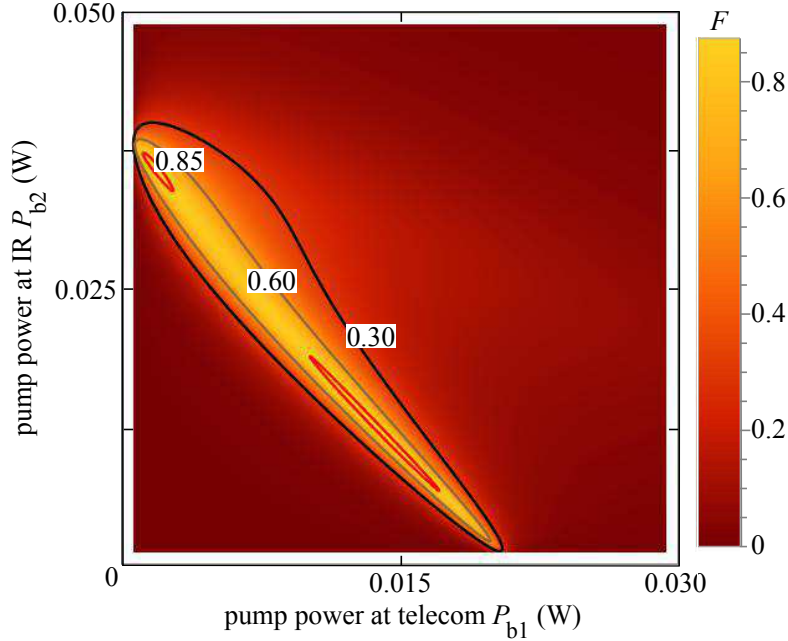


Fig. 3. Density plot of conversion efficiency F (defined in Eq. 18) over the pump powers P_{b1} and P_{b2} for the cavity system discussed in Section 3. Efficiency contours are overlaid on the plot for easy visualization. They help identify the regime of pump powers necessary for high-efficiency conversion.

and ($m_{b2} = 246, \lambda_{b2c} = 776$ nm), see Fig. 2. Finite-difference time-domain (FDTD) simulations reveal that the four modes have ultra-high radiative quality factors in excess of 10^8 . However, in actual experiments, the overall Q 's will be limited by fabrication imperfections or coupling losses. Therefore, we will examine the maximum efficiencies for two different representative cases, $Q \sim 10^5$ and $Q \sim 10^6$. For the sake of simplicity, we will assume that the overall Q 's are coupling-limited, so that $Q_i \approx Q_{si}$, $i \in \{0, s, b1, b2\}$. If this is not the case, the maximal efficiency will suffer by a factor of Q_s/Q_{ss} (see Eq. 20). The third-order nonlinear susceptibility of diamond (Kerr coefficient) is $\chi^{(3)} = 2.5 \times 10^{-21} \frac{\text{m}^2}{\text{V}^2}$ [43]. The nonlinear phase-shifts α and coupling coefficient β are found to be:

$$|\beta| = 0.120 (\mu\text{J})^{-1} \sqrt{\omega_{0c} \omega_{sc} \left(\frac{2\tau_{b1}^2}{\tau_{sb1}} \frac{2\tau_{b2}^2}{\tau_{sb2}} \right) P_{b1} P_{b2}} \quad (25)$$

$$\alpha_{0b1} = 0.114 (\mu\text{J})^{-1}, \quad \alpha_{0b2} = 0.425 (\mu\text{J})^{-1}, \quad (26)$$

$$\alpha_{sb1} = 0.215 (\mu\text{J})^{-1}, \quad \alpha_{sb2} = 0.126 (\mu\text{J})^{-1}, \quad (27)$$

$$\alpha_{bb1} = 0.099 (\mu\text{J})^{-1}, \quad \alpha_{bb2} = 0.208 (\mu\text{J})^{-1}, \quad (28)$$

$$\alpha_{b1b2} = 0.114 (\mu\text{J})^{-1}. \quad (29)$$

The maximum achievable efficiency (Eq. 20) is determined by the cooperativity factor C (Eq. 19), which can be recast as:

$$C = \frac{4g_{\text{ZPL}}^2}{\kappa_0 \gamma} \left(\sum_l \frac{4g_l^2}{\kappa_l \gamma} + \frac{\gamma^{\text{NC}}}{\gamma} \right)^{-1}, \quad (30)$$

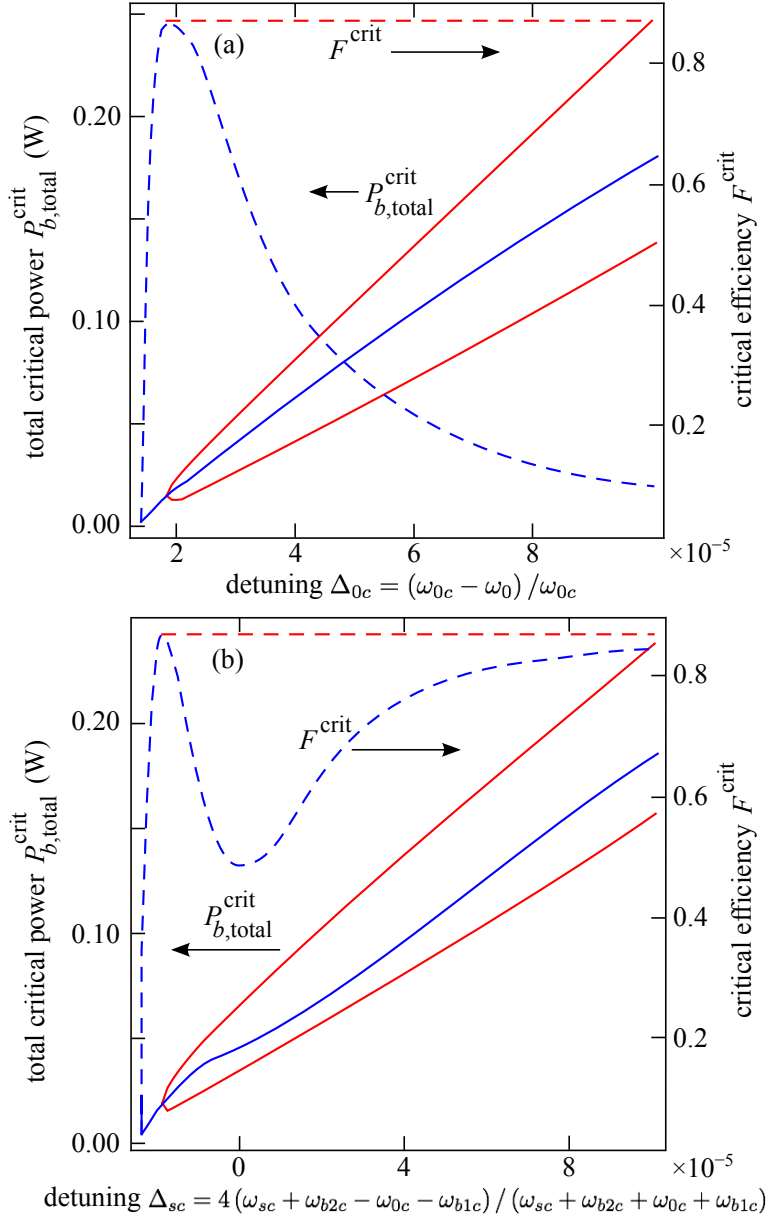


Fig. 4. (a) Critical pump power (solid lines, left-axis) and critical efficiency (dashed lines, right-axis) vs. bare-cavity fractional detuning $\Delta_{0c} = 1 - \omega_0/\omega_{0c}$. Pump power plotted here is the total pump power, $P_{b,\text{total}}^{\text{crit}} = P_{b1}^{\text{crit}} + P_{b2}^{\text{crit}}$. Two regimes can be identified: a regime with multiple critical points (light red and dark blue colors) and a regime with only one critical point (dark blue only). The former corresponds to the regime where Eq. 20 is valid and the detuning can be compensated by critical pump powers. The latter corresponds to the regime where Eq. 20 is no longer valid and the efficiency falls off rapidly with detuning. (See also text.) (b) same as above except for the detuning $\Delta_{sc} = \frac{\omega_{sc} + \omega_{b2c} - \omega_{0c} - \omega_{b1c}}{(\omega_{sc} + \omega_{b2c} + \omega_{0c} + \omega_{b1c})/4}$.

where γ is the total spontaneous decay rate of the color center in the isotropic diamond medium

in the absence of the cavity. The quantity $\sum_l \frac{4g_l^2}{\kappa_l \gamma}$ represents the relative strength of radiative decay into phonon sidebands in the presence of the ring resonator as opposed to the total decay rate in the absence of the resonator. Generally, one can compute this quantity by simulating the decay rates of all of the ring resonator modes falling within the phonon sidebands. However, in the case of SiV with a relatively weak phonon sideband, we can expect much of the sideband to be suppressed in between the ring resonator modes so that $\sum_j \frac{4g_j^2}{\kappa_j \gamma} \ll 1$. Therefore, it follows that

$$\sum_l \frac{4g_l^2}{\kappa_l \gamma} + \frac{\gamma^{\text{NC}}}{\gamma} \leq 1 \quad \text{or} \quad (31)$$

$$C \geq \frac{4g_{\text{ZPL}}^2}{\kappa_0 \gamma} \quad (32)$$

since $\frac{\gamma^{\text{NC}}}{\gamma} < 1$ in general. In our calculations, we will simply take the lower bound $C = \frac{4g_{\text{ZPL}}^2}{\kappa_0 \gamma}$. Assuming that the SiV is located at the electric-field maximum and that the dipole element is aligned with the field polarization, the coupling strength is given by $g_{\text{ZPL}} = \frac{\mu_{\text{ZPL}} |\mathbf{E}_{\text{max}}|}{\hbar}$. Spontaneous emission rate γ_{ZPL} is related to the dipole element via $\gamma_{\text{ZPL}} = \frac{n\omega_0^3 \mu_{\text{ZPL}}^2}{3\pi\epsilon_0 \hbar c^3}$. The mode volume of the 0th cavity mode is $V_{0c} = \frac{\int dV \epsilon |\mathbf{E}|^2}{\epsilon(\mathbf{r}_{\text{max}}) |\mathbf{E}_{\text{max}}|^2} = 252 \left(\frac{\lambda}{n}\right)^3$. The branching ratio of the SiV ZPL line is $\frac{\gamma_{\text{ZPL}}}{\gamma^{\text{rad}}} \approx 70\%$ [18]. A variable factor in our calculations is the internal quantum efficiency of the SiV emission (or the ratio $\gamma^{\text{rad}}/\gamma$); the current literature suggests it could vary wildly from sample to sample, from as low as 9% [44] to as high as near 100% at low temperatures [21], probably depending on material quality and method of fabrication. In Table. 1, we have computed maximal efficiencies and critical pump powers (Eq. 20 and Eqs. 22–23) for different internal quantum efficiencies and cavity lifetimes. A maximal conversion efficiency of 87% in the best possible scenario where $\gamma^{\text{rad}}/\gamma = 1$ and $Q = 10^6$ is limited by a moderate cooperativity $C \approx 211$ (see Eq. Eq. 20). However, we note that this limit only reflects the current experimental constraints on diamond fabrication ($Q \sim 10^6$); simulations have indicated that radiative quality factors can be in excess of 10^7 , in which case the maximum efficiency quickly approaches 100%.

Q	$\gamma^{\text{rad}}/\gamma$	C	P_{b1}^{crit} (W)	P_{b2}^{crit} (W)	F^{max}
10^5	0.09	2	0.110	0.424	0.26
10^5	1	21	0.255	0.507	0.65
10^6	0.09	19	3×10^{-4}	0.036	0.63
10^6	1	211	0.001	0.037	0.87

Table 1. Critical powers and efficiencies.

Next, we examine the scenario with $Q = 10^6$ and $\frac{\gamma^{\text{rad}}}{\gamma} = 1$ as the best possible performance for the given design. Figure 3 shows a density plot of the conversion efficiency (Eq. 18) as a function of the two pump powers. As observed in the figure, there exist narrow strips of high-efficiency regime ($F > 0.85$) around the pump power co-ordinates (1 mW, 35 mW) and (15 mW, 12 mW). A closer examination reveals two additional critical points (in addition to the one given in Table. 1) with efficiencies $F^{\text{crit},1} = 0.87$, $F^{\text{crit},2} = 0.82$ and pump powers $P_{b1}^{\text{crit},1} \approx 14$ mW, $P_{b1}^{\text{crit},2} \approx 11$ mW and $P_{b2}^{\text{crit},1} \approx 5$ mW, $P_{b2}^{\text{crit},2} \approx 28$ mW respectively. In contrast to the tabulated critical point, these extra points have a small but non-vanishing phase mismatch $\delta \neq 0$ and are obtained from a complete solution of the algebraic equation (Eq. 21)

or from the direct optimization over pump powers (Eq. 24). The existence of multiple critical points is a result of a complex interplay between two competing decay channels, (i) the decay of the excited state with the concomitant photon release into mode 0 and (ii) the conversion of the released photon to the telecom mode s . If the leakage from mode 0 to s is too strong, no cavity enhanced emission occurs, degrading the efficiency, whereas if this leakage is too weak, nonlinear conversion efficiency vanishes. These decay rates are controlled by the nonlinear detunings, δ_{0c} , δ_{sc} , and nonlinear coupling β parameters, which are in turn controlled by the input powers. Specifically, δ_{0c} tends to inhibit the emitter $\rightarrow 0$ decay channel, δ_{sc} tends to inhibit the $0 \rightarrow s$ decay channel, and β tends to enhance the $0 \rightarrow s$ decay channel. The complex interplay between these parameters introduces multiple critical points over the P_{b1} - P_{b2} plane.

As we have shown above, the nonlinear detunings δ 's are directly controlled by incident pump powers, which can, therefore, be appropriately chosen to ensure maximum conversion efficiency. The magnitudes of the critical pump powers in turn depend on how much frequency detuning the system begins with. Theoretically, the cavity parameters can be numerically optimized so that these detunings are made as small as possible. However, random errors in the actual fabrication process can introduce significant deviations from any designated cavity frequencies. Therefore, it is advisable to consider the effects of frequency detunings due to possible variations in ring radius R and height h . For this purpose, we define the *bare*-cavity fractional detunings: $\Delta_{0c} = 1 - \omega_0/\omega_{0c}$, $\Delta_{sc} = \frac{\omega_{sc} + \omega_{b2c} - \omega_{0c} - \omega_{sc}}{(\omega_{sc} + \omega_{b2c} + \omega_{0c} + \omega_{b1c})/4}$. Figure 4 shows the *total* critical power $P_{b,\text{total}}^{\text{crit}} = P_{b1}^{\text{crit}} + P_{b2}^{\text{crit}}$ and corresponding critical efficiencies F^{crit} as a function of Δ_{0c} (Fig. 4(a)) and Δ_{sc} (Fig. 4(b)). (Note that F^{crit} denotes *all* critical points, including local and global maxima.) Here, Δ_{0c} is varied by varying ω_0 while keeping all other frequencies fixed, and Δ_{sc} is varied by varying ω_{sc} . We find that generally there exist two regimes of operation: a regime where there are two critical efficiencies, one at $F^{\text{crit}} = 0.87$ (light red dashed line) and the other at $F^{\text{crit}} < 0.87$ (dark blue dashed line), and a regime where only the smaller efficiency survives, $F^{\text{crit}} < 0.87$ (dark blue dashed line). These two regimes clearly reflect to what extent the detunings can be compensated for by incident pump powers. In the first regime, the detunings can be completely compensated and the maximal efficiency is only limited by cooperativity C . The global maximum is explicitly computed from Eq. 21 as $F^{\text{crit}} = 0.87$ and can be realized by applying either of the two critical powers (light red solid lines) corresponding to either vanishing or non-vanishing δ 's. The required power then grows with the increasing Δ 's while the global maximal efficiency stays the same. In the second regime, Eq. 21 breaks down (leading to complex solutions), and the critical parameters can only be computed from setting $\frac{\partial F}{\partial P_{b1}} = 0$, $\frac{\partial F}{\partial P_{b2}} = 0$. Clearly, in this regime, the detunings cannot be fully compensated so that the maximal efficiency falls off rapidly.

4. Difference frequency generation

So far, we have tailored our resonator design to the FWM-BS process. Designing a cavity for the alternative scheme of DFG is significantly more challenging since the pump modes must be designed at a wavelength of $\sim 3\mu\text{m}$, more than thrice that of the SiV emitter, so that the generated signal falls within the telecom band (see Fig. 5). For these wavelengths, phase-matching can only be achieved by utilizing higher-order waveguide modes; as a consequence, the overlap between the cavity modes suffers, degrading the β coefficient. Nevertheless, with the help of the phase-matching method described in Appendix C, we were able to obtain realistic designs that still yield high efficiencies at reasonable pump powers. Such a design is shown in Fig. 5.

In order to separate TE-like and TM-like bands as wide as possible, we choose a shallow etch angle of $\theta = 70^\circ$; the radius and height are $34\mu\text{m}$ and 463nm respectively. The waveguide dimensions are chosen to be larger than the previous design for FWM-BS in order to host high-Q modes at very different wavelengths: ($m_0 = 461, \lambda_{0c} = 0.738\mu\text{m}$), ($m_s = 235, \lambda_s = 1.567\mu\text{m}$)

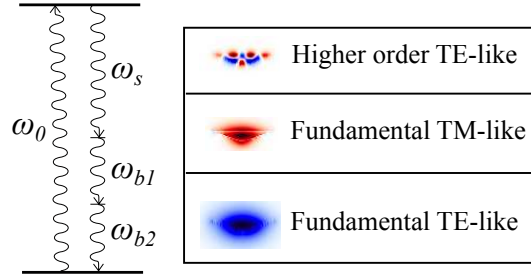


Fig. 5. Left panel: a diagrammatic representation of difference frequency generation process (DFG), Right panel: E_r and E_z components of a higher-order TE-like mode (for the emitter photon), a fundamental TM0-like mode (for the signal photon) and a fundamental TE0-like mode (for the pump photons). TE and TM characters of the modes are ill-defined since the mirror symmetry in z (the out-of-plane direction perpendicular to the plane of the resonator) is strongly broken. Each mode possesses appreciable in-plane and out-of-plane electric field components, which lead to a non-vanishing β (see Eq. 4).

and ($m_{b1} = m_{b2} = m_b = 113, \lambda_{b1c} = \lambda_{b2c} = \lambda_b = 2.789 \mu\text{m}$). (Note the pumps are degenerate so that we are actually dealing with three cavity modes instead of four.) Here, it should be noted that even though we make use of two TE-like modes and one TM-like modes (see Fig. 5), we found that the overlap β does not vanish because TE and TM characters of the modes are ill-defined for the triangular waveguide, all the modes having significant in-plane and out-of-plane components. From FDTD, radiation Q's are found to be in excess of 10^8 ; we assume operational Q's of 10^6 . The mode volume of the 0th cavity mode is $V_{0c} \approx 1052 \left(\frac{\lambda}{n}\right)^3$, yielding a cooperativity factor of about 50 (assuming 100% internal quantum efficiency of the emitter). The analysis of DFG exactly follows that of DFWM, except that we interchange $\omega_{b1} \rightarrow -\omega_{b1}$ and $\vec{E}_{b1} \rightarrow \vec{E}_{b1}^*$. While the self- and cross-phase modulation coefficients are comparable to those in the case of FWM-BS, the overlap coefficient is about $2.5 \times 10^{-4} (\mu\text{J})^{-1}$, which is more than two orders of magnitude smaller than in the case of FWM-BS. With these numbers in place, we calculated the critical efficiency and powers which are found to be 64% and $\sim 1 \text{ W}$.

5. Conclusion

We have presented efficiency and power requirements for frequency down-conversion of SiV single photons to telecom wavelengths. Our cavity designs are tailored for a potential all-diamond monolithic approach which directly utilizes the nonlinear optical properties of diamond. This stands in contrast to more common hybrid approaches [35] which employs an external nonlinear material, usually a $\chi^{(2)}$ medium, for frequency conversion. Although the power requirements (on the order of 10 – 100 mW) are greater for all-diamond systems since the inherent $\chi^{(3)}$ nonlinearity of diamond is weaker, the maximum-achievable efficiencies are comparable to $\chi^{(2)}$ -based systems, for example Ref. [35]. The advantage of a potential all-diamond approach is the superior quality of the native emitters in monolithic diamond as well as relative ease of fabrication, scalability and high throughput promised by the advent of angle-etched techniques [45].

A. Nonlinear terms in Hamiltonian

The perturbative nonlinear interaction energy is given by [46]

$$\delta U^{\text{NL}} = -\frac{1}{2} \int dV \mathbf{E}^*(\omega) \cdot \mathbf{P}^{\text{NL}}(\omega). \quad (33)$$

There are detailed theoretical methods on how to rigorously quantize a nonlinear system [38, 46] but we will not follow those arguments here since we are only interested in the perturbative regime.

The nonlinear polarization for four-wave mixing Bragg scattering process is given in [43],

$$P_i^{\text{NL}}(\omega_s) = D \epsilon_0 \chi_{ijkl}^{(3)}(\omega_s; \omega_0, \omega_{b1}, -\omega_{b2}) E_{0j} E_{b1k} E_{b2l}^*, \quad (34)$$

where D is the permutation factor and in this case $D = 6$ [43]. The electric fields should be normalized as

$$\int dV \mathbf{E}_\mu^*(\omega) \cdot \epsilon \mathbf{E}_\mu(\omega) = \frac{1}{2} \hbar \omega_\mu \quad (35)$$

$$\int dV \mathbf{E}_b^*(\omega) \cdot \epsilon \mathbf{E}_b(\omega) = \frac{1}{2} |a_b|^2 \quad (36)$$

In an isotropic medium like diamond, the components of the nonlinear susceptibility tensor are given by $\chi_{ijkl} = \chi_{xyxy} \delta_{ij} \delta_{kl} + \chi_{xyxy} \delta_{ik} \delta_{jl} + \chi_{xyxy} \delta_{il} \delta_{jk}$. Substituting Eq. 34 in Eq. 33 leads to the expression for β as given in Eq. 4. Similar calculations can be performed to yield the expressions for α 's, Eqs. 5–7. For wavelengths of interest which are well into non-resonant regime, full-permutation symmetry holds [43] and we approximate that $\chi_{xyxy} \approx \chi_{xyxy} \approx \chi_{xyxy} \approx \chi_{xxxx}/3 = \chi^{(3)}/3$. For diamond, $\chi^{(3)} = 2.5 \times 10^{-21} \text{ m}^2/\text{V}^2$ [43].

B. Adiabatic elimination

When Ω is sufficiently small, c_r becomes the slowest dynamical variable in the system leading the other three. In this case, c_e , c_0 , c_s , c_l all decay approximately at the same rate as c_r . In other words, c_e , c_0 , c_s , c_l are simply proportional to c_r (they follow c_r except for a constant pre-factor). To obtain these proportionalities, we can formally set \dot{c}_e , \dot{c}_0 , \dot{c}_s , $\dot{c}_l = 0$ individually (adiabatic elimination) and solve for these variables as functions of c_r . This leads to a simple rate equation for c_r :

$$\dot{c}_r = (i\delta_r - \frac{\kappa_r}{2})c_r, \quad (37)$$

where δ_r is some phase factor giving rise to unitary oscillations and κ_r is the effective rate of population loss predicted from the state $|r\rangle$. The latter is given by

$$\kappa_r = \frac{|\Omega|^2}{\gamma} \left(1 - \frac{4|\beta|^2 C \kappa_0 \kappa_s}{16|\beta|^2 + 8|\beta|^2 (\kappa_0 \kappa_s (1+C) - 4\delta_{0c} \delta_{sc}) + (4\delta_{0c}^2 + (1+C)^2 \kappa_0^2) (4\delta_{sc}^2 + \kappa_s^2)} \right). \quad (38)$$

Self-consistency of adiabatic elimination requires that the population loss out of r does not exceed the rate κ_s with which a photon can leak out through the cavity mode s , $\kappa_r < \kappa_s$. Additionally, in our calculations, we have rigorously checked the validity of adiabatic elimination by direct comparison with exact numerical integration of Eqs. 10–16, using $|\Omega| \sim 0.1 \kappa_0$.

C. Ring resonator design

We begin by examining the modes of an infinite straight waveguide having a triangular cross-section. Specifically, we chose an etch-angle of 60° and a height of $0.25a$ where a is an arbitrary normalization length to be chosen later. The modes of the waveguides can be quickly computed by standard band structure solvers; for our simulations, we use the freely-available open-source MPB [47] which compute eigenfrequencies f (in units of c/a) at specified k 's (in units of $2\pi/a$). We select two bands which are far-separated in frequency but still have significant overlap; such bands are readily afforded by the fundamental TE₀ and fundamental TM₀ modes (see the inset of Fig. 6). Next, we define the phase mismatch as a function of frequencies (for the case of FWM-BS)

$$\delta k(f_1, f_2, f_3, f_4) = k_1 + k_2 - k_3 - k_4. \quad (39)$$

We want two of the frequencies, say, f_2 and f_4 to lie within the NIR band and the other two, f_1 and f_3 , within the telecom band. Therefore, we identify: $k_1 = k_{\text{TE}_0}(f_1)$, $k_2 = k_{\text{TM}_0}(f_2)$, $k_3 = k_{\text{TE}_0}(f_3)$, $k_4 = k_{\text{TM}_0}(f_4)$.

δk is a function of four independent variables f_1, f_2, f_3, f_4 which is hard to visualize. We subject the frequencies to the constraint $f_1 + f_2 = f_3 + f_4$. In order to reduce the number of free variables further, we make f_3 a function of f_1 and f_2 , i.e., $f_3 = f_3(f_1, f_2)$. This also makes f_4 a function of f_1 and f_2 . The functional form of f_3 can be chosen arbitrarily. A simple intuitive choice would be to set $f_3 = f_1 - \delta f$ for some offset δf . Since the number of variables has been reduced to two, we are ready to visualize δk . Choosing $df = 0.1$, we plotted a contour of $\delta k = 0$ over the f_1 vs. f_2 plane (see Fig. 6). Each point along the contour yields four waveguide modes with frequencies that are perfectly phase-matched for an efficient FWM-BS process. In particular, we chose a point on the contour (red circle in Fig. 6): $f_1 = 0.95$, $f_2 = 2.00$, $f_3 = 0.85$, $f_4 = 2.10$. It is easily noticed that f_4 and f_1 have the approximate ratio as two frequencies from SiV and telecom bands. So we identify $f_4 \frac{c}{a} = f_0 = \frac{c}{0.738 \mu\text{m}}$, yielding $a = 1.55 \mu\text{m}$ and $f_s = f_1 \frac{c}{a} = \frac{c}{1.63 \mu\text{m}}$. This also specifies the height of the waveguide, $h \approx 390 \text{ nm}$. Remembering that ring resonances satisfy the condition $m_i = 2\pi R n_{\text{eff},i} f_i$, $i \in \{0, s, b1, b2\}$, we can find an optimal R which makes m_i an integer (or closest to an integer) for each of the four modes. We found that $R \sim 14.7 \mu\text{m}$ approximately gives $m_0 = 262$, $m_s = 95$, $m_{b1} = 79$, $m_{b2} = 246$, also satisfying the condition $m_0 + m_{b1} = m_s + m_{b2}$. Now we can proceed to simulate the ring resonator via full-scale FDTD, using the predicted design parameters. A quick inexpensive search (on the order of ten iterations) in the vicinity of the above parameters directly yields the design given in Section 3.

A similar procedure is followed to design a cavity for DFG except that the angle is made shallower $\theta = 70^\circ$. We found that the 8th order TE-like band together with fundamental TE-like and TM-like bands yield a regime of phase-matched frequencies (not shown) similar to the one depicted in Fig. 6, thereby identifying appropriate parameters which lead to the resonator design of Section 4 after a quick numerical search.

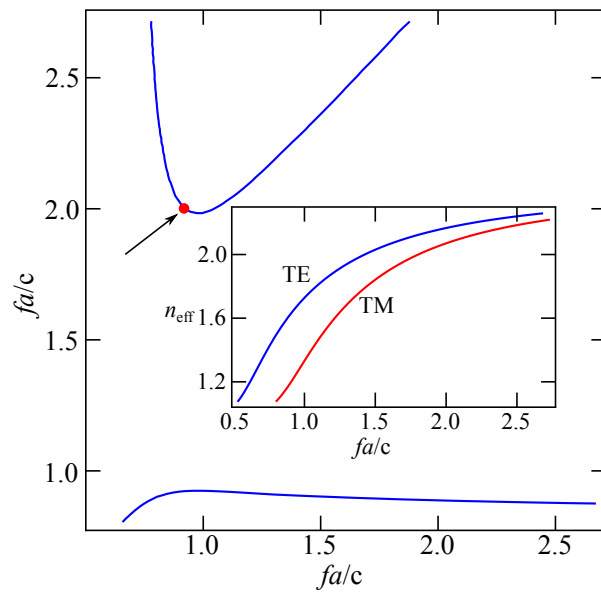


Fig. 6. Phase-matching diagram for the FWM-BS process in a triangular waveguide of $h = 0.25a$ and $\theta = 60^\circ$. The red circle indicates the frequencies used in the design of ring resonator. Inset: fundamental TE₀ and TM₀ bands computed by MPB. a is an arbitrary normalization length to be chosen later (see text).